Torques on Spheroidal Silicate Grains Exposed to Anisotropic Interstellar Radiation Fields

Joseph C. Weingartner & Margaret E. Jordan

Department of Physics and Astronomy, George Mason University, MSN 3F3, 4400 University Drive, Fairfax, VA 22030, USA

ABSTRACT

Radiative torques, due to the absorption and scattering of starlight, are thought to play a major role in the alignment of grains with the interstellar magnetic field. The absorption of radiation also gives rise to recoil torques, associated with the photoelectric effect and photodesorption. The recoil torques are much more difficult to model and compute than the direct radiative torque. Here, we consider the relatively simple case of a spheroidal grain. Given our best estimates for the photoelectric yield and other relevant grain physical properties, we find that the recoil torques contribute at the $\approx 10\%$ level or less compared with the direct radiative torque. We recommend that the recoil torques not be included in models of radiation-driven grain alignment at this time. However, additional experimental characterization of the surface properties and photoelectric yield for sub-micron grains is needed to better quantify the magnitude of these torques.

Subject headings: ISM: dust

1. Introduction

As starlight traverses the dusty interstellar medium (ISM), it acquires a partial linear polarization, due to dichroic extinction. Grains are non-spherical and are more effective at attenuating radiation polarized along their "long" axes, which tend to align along the same direction in space. Despite decades of investigation, the alignment mechanism is still not fully understood; see Lazarian (2003), Roberge (2004), and Lazarian (2007) for recent reviews.

Radiative torques, due to the absorption and scattering of starlight, appear to play a major role in grain alignment (Draine & Weingartner 1996, 1997). If the incident radiation field is anisotropic, then radiative torques can directly align grains, at least for the few grain shapes that have been investigated so far. A detailed investigation, incorporating a large suite of shapes, is needed in order to fully assess the viabilty of radiation-driven alignment. Although the alignment is not due to magnetic torques in this scenario, the observed polarization is nevertheless correlated with the interstellar magnetic field direction, since the grains have magnetic dipole moments lying along their

spin axes and thus precess rapidly about the field direction (Martin 1971; Dolginov & Mytrophanov 1976).

In addition to the direct torque due to absorption and scattering, there are also recoil torques, associated with photoelectric emission and photodesorption. In the latter process, adsorbed atoms or molecules (i.e., gas-phase particles that have stuck to the grain surface after colliding with it) are ejected back into the gas after an absorbed photon breaks the bond between the adsorbed particle and the surface. So far, photoelectric and photodesorption torques associated with anisotropic radiation have not been considered. However, one expects that they could be significant compared with the direct radiative torque, since Weingartner & Draine (2001a) found that the photoelectric and photodesorption *forces* can be comparable to the direct radiation pressure force in some interstellar environments.

Here, we estimate the photoelectric torque for two simple grain shapes, namely, prolate and oblate spheroids with axis ratios of 1.5. We also estimate the maximum magnitude for the photodesorption torque. We consider grains with silicate composition and $a_{\rm eff} = 0.2\mu$m ($a_{\rm eff}$ is the radius of a sphere with equal volume); such grains are known to be well-aligned in the diffuse ISM (e.g., Kim & Martin 1995).

Photoelectrons typically originate within $\sim 10\,$Å of the grain surface and the ejection rate is proportional to the electric intensity $|\mathbf{E}|^2$. Thus, the field inside the grain must be determined to within high resolution (10 Å out of 0.2μm) in order to compute the photoelectric torque, unless the near-surface field remains fairly constant on larger length scales. Draine & Weingartner (1996, 1997) computed radiative torques using the discrete dipole approximation, in which the grain is approximated as a set of polarizable points. The size of the dipole array needed to achieve a resolution of 10 Å out of 0.2μm is prohibitive. Thus, we adopt the point matching method (PMM), which can achieve high resolution at relatively low computational cost. In this approach, the internal and scattered fields are expanded in vector spherical wave functions and the expansion coefficients are found by imposing boundary conditions at a set of discrete points on the grain surface.

The PMM simplifies considerably for grains with azimuthal symmetry; this motivated our choice of spheroids. However, these grains are too symmetric for radiation torques (including the recoil torques) to yield alignment, if the surface properties are uniform. The purpose of this paper is simply to estimate the magnitude of the recoil torques relative to the direct radiative torque, in order to determine whether or not recoil torques need to be included in future studies of radiation-driven alignment. Detailed scattering computations are required even for this simple goal, since the wavelength of the incident radiation is comparable to the grain size. In this case, the internal electric intensity cannot be simply estimated using geometrical optics and an attenuation coefficient.

In §2, we describe our implementation of the PMM, which is based on the treatments of Morrison & Cross (1974) and Al-Rizzo & Tranquilla (1995). §3 describes the computation of efficiency factors for extinction, scattering, radiation pressure, and radiative torque. Readers who

are interested only in the results should skip §§2 and 3.1. In §4, we describe our simple model for the photoelectric force and torque and present computational results. §5 briefly examines the photodesorption torque. We conclude (§6) with a discussion of the implications of these estimates for future grain alignment studies.

2. Point Matching Method

In spherical coordinates, solutions of the vector Helmholtz equation are given by $\mathbf{M}_{nm}(r,\theta,\phi)$ and $\mathbf{N}_{nm}(r,\theta,\phi)$, with

$$M_r(r,\theta,\phi) = 0 \tag{1}$$

$$M_\theta(r,\theta,\phi) = \frac{im}{\sin\theta}\, Z(kr)\, P(\cos\theta)\, e^{im\phi} \tag{2}$$

$$M_\phi(r,\theta,\phi) = \sin\theta\, Z(kr)\, P'(\cos\theta)\, e^{im\phi} \tag{3}$$

$$N_r(r,\theta,\phi) = \frac{n\,(n+1)}{kr}\, Z(kr)\, P(\cos\theta)\, e^{im\phi} \tag{4}$$

$$N_\theta(r,\theta,\phi) = -\sin\theta\, \left[Z'(kr) + \frac{Z(kr)}{kr}\right]\, P'(\cos\theta)\, e^{im\phi} \tag{5}$$

$$N_\phi(r,\theta,\phi) = \frac{im}{\sin\theta}\, \left[Z'(kr) + \frac{Z(kr)}{kr}\right]\, P(\cos\theta)\, e^{im\phi} \tag{6}$$

where $P(\cos\theta) = P_n^{|m|}(\cos\theta)$, $P'(\cos\theta) = dP_n^{|m|}(\cos\theta)/d(\cos\theta)$, k is the wave number ($k = k_0 \equiv 2\pi/\lambda$ outside the grain and $k = n_{\rm ref} k_0$ inside the grain, where $n_{\rm ref}$ is the grain index of refraction and λ is the wavelength of the incident radiation), $Z(kr) = j_n(kr)$ (spherical Bessel function of the first kind) inside the grain and $Z(kr) = h_n^{(1)}(k_0 r)$ (spherical Hankel function of the first kind) outside the grain, and $Z'(kr) = dZ(kr)/d(kr)$. We adopt Jackson's (1999) convention for associated Legendre polynomials $P_n^m(\cos\theta)$.

The scattered electric ($\mathbf{E}_{\rm sca}$) and magnetic ($\mathbf{H}_{\rm sca}$) fields are given by

$$\mathbf{E}_{\rm sca} = \sum_{n=1}^{\infty} \sum_{m=-n}^{n} \left[a_{nm}(1)\, \mathbf{N}_{nm}^{(s)} + a_{nm}(2)\, \mathbf{M}_{nm}^{(s)}\right] \tag{7}$$

$$\mathbf{H}_{\rm sca} = -i \sum_{n=1}^{\infty} \sum_{m=-n}^{n} \left[a_{nm}(1)\, \mathbf{M}_{nm}^{(s)} + a_{nm}(2)\, \mathbf{N}_{nm}^{(s)}\right] \tag{8}$$

and the internal fields are given by

$$\mathbf{E}_{\rm int} = \sum_{n=1}^{\infty} \sum_{m=-n}^{n} \left[a_{nm}(3)\, \mathbf{N}_{nm}^{(w)} + a_{nm}(4)\, \mathbf{M}_{nm}^{(w)}\right] \tag{9}$$

$$\mathbf{H}_{\rm int} = -i n_{\rm ref} \sum_{n=1}^{\infty} \sum_{m=-n}^{n} \left[a_{nm}(3)\, \mathbf{M}_{nm}^{(w)} + a_{nm}(4)\, \mathbf{N}_{nm}^{(w)}\right] \tag{10}$$

where superscripts (s) and (w) refer to evaluation in the grain exterior and interior, respectively.

We will take the z-axis as the symmetry axis of the spheroidal grain and assume that the incident radiation field wave vector $\mathbf{k}_0$ lies in the x-z plane with $\mathbf{k}_0 = k_0(\cos\theta_0\,\hat{z} - \sin\theta_0\,\hat{x})$. We also adopt unit amplitude for the incident electric field $\mathbf{E}_{\rm inc}$. When $\mathbf{E}_{\rm inc}$ lies in the x-z plane (TM mode),

$$\mathbf{E}_{\rm inc,\,TM} = [\hat{r}(\cos\theta_0\sin\theta\cos\phi+\sin\theta_0\cos\theta)+\hat{\theta}(\cos\theta_0\cos\theta\cos\phi-\sin\theta_0\sin\theta)-\hat{\phi}\cos\theta_0\sin\phi]\,\exp(i\mathbf{k}_0\cdot\mathbf{r}) \quad , \tag{11}$$

$$\mathbf{H}_{\rm inc,\,TM} = [\hat{r}\sin\theta\sin\phi + \hat{\theta}\cos\theta\sin\phi + \hat{\phi}\cos\phi]\,\exp(i\mathbf{k}_0\cdot\mathbf{r}) \tag{12}$$

with

$$\mathbf{k}_0\cdot\mathbf{r} = k_0 r(\cos\theta_0\cos\theta - \sin\theta_0\sin\theta\cos\phi) \quad . \tag{13}$$

For the orthogonal polarization state (TE mode),

$$\mathbf{E}_{\rm inc,\,TE} = \mathbf{H}_{\rm inc,\,TM} \quad ; \quad \mathbf{H}_{\rm inc,\,TE} = -\mathbf{E}_{\rm inc,\,TM} \quad . \tag{14}$$

At the surface, the tangential components of $\mathbf{E}$ and $\mathbf{H}$ and the normal components of $\mathbf{D} \equiv \epsilon\mathbf{E}$ (ϵ is the dielectric function) and $\mathbf{H}$ are continuous.

For the grain surface, the radius r as a function of polar angle θ is given by

$$r(\theta) = a\left[\cos^2\theta + \zeta^2\sin^2\theta\right]^{-1/2} \quad . \tag{15}$$

For prolate grains, a is the semimajor axis length and $\zeta > 1$ is the ratio of the semimajor axis length to the semiminor axis length. For oblate grains, a is the semiminor axis length and $\zeta < 1$ is the ratio of the semiminor axis length to semimajor axis length. Given the radius $a_{\rm eff}$ of a sphere of equal volume, $a = a_{\rm eff}\,\zeta^{2/3}$.

In this case, the boundary conditions on the tangential field components become

$$E_{{\rm inc},\phi} + E_{{\rm sca},\phi} = E_{{\rm int},\phi} \tag{16}$$

$$H_{{\rm inc},\phi} + H_{{\rm sca},\phi} = H_{{\rm int},\phi} \tag{17}$$

$$(1-\zeta^2)\sin\theta\cos\theta\,(E_{{\rm inc},r} + E_{{\rm sca},r} - E_{{\rm int},r}) + (\cos^2\theta + \zeta^2\sin^2\theta)\,(E_{{\rm inc},\theta} + E_{{\rm sca},\theta} - E_{{\rm int},\theta}) = 0 \tag{18}$$

$$(1-\zeta^2)\sin\theta\cos\theta\,(H_{{\rm inc},r} + H_{{\rm sca},r} - H_{{\rm int},r}) + (\cos^2\theta + \zeta^2\sin^2\theta)\,(H_{{\rm inc},\theta} + H_{{\rm sca},\theta} - H_{{\rm int},\theta}) = 0 \quad . \tag{19}$$

The boundary conditions on the normal field components are

$$(\cos^2\theta + \zeta^2\sin^2\theta)\,(D_{{\rm inc},r} + D_{{\rm sca},r} - D_{{\rm int},r}) + (\zeta^2-1)\sin\theta\cos\theta\,(D_{{\rm inc},\theta} + D_{{\rm sca},\theta} - D_{{\rm int},\theta}) = 0 \tag{20}$$

$$(\cos^2\theta + \zeta^2\sin^2\theta)\,(H_{{\rm inc},r} + H_{{\rm sca},r} - H_{{\rm int},r}) + (\zeta^2-1)\sin\theta\cos\theta\,(H_{{\rm inc},\theta} + H_{{\rm sca},\theta} - H_{{\rm int},\theta}) = 0 \quad . \tag{21}$$

The incident radiation field can be expressed as follows:

$$E_{r,{\rm TM}} = \exp(ik_0 r\cos\theta_0\cos\theta)\sum_{m=-\infty}^{\infty} i^m\,[J_m(u)\sin\theta_0\cos\theta - iJ'_m(u)\cos\theta_0\sin\theta]\,\exp(im\phi) \tag{22}$$

$$E_{\theta,\mathrm{TM}} = -\exp(ik_0 r\cos\theta_0\cos\theta)\sum_{m=-\infty}^{\infty} i^m\left[J_m(u)\sin\theta_0\sin\theta + iJ'_m(u)\cos\theta_0\cos\theta\right]\exp(im\phi) \quad (23)$$

$$E_{\phi,\mathrm{TM}} = \exp(ik_0 r\cos\theta_0\cos\theta)\,\cos\theta_0\sum_{m=-\infty}^{\infty} i^m m u^{-1}J_m(u)\exp(im\phi) \quad (24)$$

$$H_{r,\mathrm{TM}} = -\sin\theta\,\exp(ik_0 r\cos\theta_0\cos\theta)\sum_{m=-\infty}^{\infty} i^m m u^{-1}J_m(u)\exp(im\phi) \quad (25)$$

$$H_{\theta,\mathrm{TM}} = -\cos\theta\,\exp(ik_0 r\cos\theta_0\cos\theta)\sum_{m=-\infty}^{\infty} i^m m u^{-1}J_m(u)\exp(im\phi) \quad (26)$$

$$H_{\phi,\mathrm{TM}} = -\exp(ik_0 r\cos\theta_0\cos\theta)\sum_{m=-\infty}^{\infty} i^{m+1}J'_m(u)\exp(im\phi) \quad (27)$$

with $u = -k_0 r\sin\theta_0\sin\theta$, $J_m(u)$ the Bessel function, and $J'_m(u) = dJ_m(u)/du$.

To find the expansion coefficients a_{nm}, the field expressions in equations (7) through (10) and (22) through (27) are substituted into the boundary conditions (16) through (19). In the resulting equations, each term contains a factor $\exp(im\phi)$ and no other ϕ-dependence. Multiplying by $\exp(-im'\phi)$ and integrating over ϕ, we find the following equations, which much be satisfied for each value of m, θ, and $i = 1$ through 4:

$$\sum_{n=|m|}^{\infty}\sum_{j=1}^{4} C_{nm}(i,j)\cdot a_{nm}(j) = D_m(i) \quad (28)$$

with

$$C_{nm}(1,1) = (1-\zeta^2)\sin\theta\cos\theta N^{(s)}_{nm,r}(\phi=0) + (\cos^2\theta + \zeta^2\sin^2\theta)N^{(s)}_{nm,\theta}(\phi=0) \quad (29)$$

$$C_{nm}(1,2) = (\cos^2\theta + \zeta^2\sin^2\theta)M^{(s)}_{nm,\theta}(\phi=0) \quad (30)$$

$$C_{nm}(1,3) = -(1-\zeta^2)\sin\theta\cos\theta N^{(w)}_{nm,r}(\phi=0) - (\cos^2\theta + \zeta^2\sin^2\theta)N^{(w)}_{nm,\theta}(\phi=0) \quad (31)$$

$$C_{nm}(1,4) = -(\cos^2\theta + \zeta^2\sin^2\theta)M^{(w)}_{nm,\theta}(\phi=0) \quad (32)$$

$$C_{nm}(2,1) = N^{(s)}_{nm,\phi}(\phi=0) \quad (33)$$

$$C_{nm}(2,2) = M^{(s)}_{nm,\phi}(\phi=0) \quad (34)$$

$$C_{nm}(2,3) = -N^{(w)}_{nm,\phi}(\phi=0) \quad (35)$$

$$C_{nm}(2,4) = -M^{(w)}_{nm,\phi}(\phi=0) \quad (36)$$

$$C_{nm}(3,1) = C_{nm}(1,2) \quad (37)$$

$$C_{nm}(3,2) = C_{nm}(1,1) \quad (38)$$

$$C_{nm}(3,3) = n_{\mathrm{ref}}C_{nm}(1,4) \quad (39)$$

$$C_{nm}(3,4) = n_{\rm ref} C_{nm}(1,3) \tag{40}$$

$$C_{nm}(4,1) = C_{nm}(2,2) \tag{41}$$

$$C_{nm}(4,2) = C_{nm}(2,1) \tag{42}$$

$$C_{nm}(4,3) = n_{\rm ref} C_{nm}(2,4) \tag{43}$$

$$C_{nm}(4,4) = n_{\rm ref} C_{nm}(2,3) \tag{44}$$

and

$$D_m(1) = i^m [J_m(u) \sin\theta_0 \sin\theta \zeta^2 + i J'_m(u) \cos\theta_0 \cos\theta] \exp(ik_0 r \cos\theta_0 \cos\theta) \tag{45}$$

$$D_m(2) = -i^m m u^{-1} \cos\theta_0 J_m(u) \exp(ik_0 r \cos\theta_0 \cos\theta) \tag{46}$$

$$D_m(3) = i^{m+1} m u^{-1} J_m(u) \cos\theta \exp(ik_0 r \cos\theta_0 \cos\theta) \tag{47}$$

$$D_m(4) = -i^m J'_m(u) \exp(ik_0 r \cos\theta_0 \cos\theta) \quad . \tag{48}$$

In practice, we impose an upper cutoff for $|m|$, $m_{\rm max}$, and for n, $n_{\rm max}$. For each m, we find the expansion coefficients a_{nm} by performing a least-squares minimization of

$$\left\| \sum_{\theta,i} \left\{ \sum_{n=|m|}^{n_{\rm max}} \sum_j [C_{nm}(i,j;\theta) \cdot a_{nm}(j) - D_m(i;\theta)] \right\} \right\|^2 \tag{49}$$

We generally take $2n_{\rm max}$ to $3n_{\rm max}$ values of θ, evenly spaced in $\cos\theta$.

The design matrix for the least-squares problem is a $4n_\theta$ by $4(n_{\rm max} - |m| + 1)$ matrix, made up from $C_{nm}(i,j;\theta)$, and does not depend on θ_0. We first apply a QR-decomposition to the design matrix. The computational time required to then complete the solution is small compared with the time to accomplish the factorization. Thus, several additional values of θ_0 can be treated without substantially increasing the computational time. The matrix equations often exhibit serious ill-conditioning. We work around this problem by implementing the solution using Mathematica, which supports arbitrary-precision arithmetic.

Note that, when m changes sign, $C(1,2)$, $C(1,4)$, $C(2,1)$, $C(2,3)$, $C(3,1)$, $C(3,3)$, $C(4,2)$, $C(4,4)$, $D(2)$, and $D(3)$ change sign, while the other components retain their sign. Thus, for the TM mode,

$$a_{n,-m}(1) = a_{n,m}(1) \;\; ; \;\; a_{n,-m}(2) = -a_{n,m}(2) \;\; ; \;\; a_{n,-m}(3) = a_{n,m}(3) \;\; ; \;\; a_{n,-m}(4) = -a_{n,m}(4) \quad \text{(TM)} \tag{50}$$

and for the TE mode,

$$a_{n,-m}(1) = -a_{n,m}(1) \;\; ; \;\; a_{n,-m}(2) = a_{n,m}(2) \;\; ; \;\; a_{n,-m}(3) = -a_{n,m}(3) \;\; ; \;\; a_{n,-m}(4) = a_{n,m}(4) \quad \text{(TE)} \tag{51}$$

As a result, it is not necessary to separately compute the expansion coefficients for $m < 0$. When $m = 0$, $a_{n,m}(2)$ and $a_{n,m}(4)$ equal zero for the TM mode and $a_{n,m}(1)$ and $a_{n,m}(3)$ equal zero for the TE mode.

When $\theta_0 = 0$, all of the azimuthal modes vanish, except for those with $m = \pm 1$. In this case, the above expressions for the incident field components (eqs. 22–27) contain the ill-defined terms $J'_m(u)$ and $J_m(u)/u$ with $u = 0$. Equations (45) through (48) must be replaced with

$$D_1(1) = D_1(3) = -\frac{1}{2}\cos\theta \exp(ik_0 r\cos\theta) \tag{52}$$

$$D_1(2) = D_1(4) = -\frac{i}{2}\exp(ik_0 r\cos\theta) \quad . \tag{53}$$

To verify the solution, we check that the boundary conditions (16) through (21) are indeed satisfied. This is particularly powerful for conditions (20) and (21), since these are not used in the solution. In addition, we check that the field intensity exhibits the following symmetry: $|\mathbf{E}|^2(2\pi - \phi) = |\mathbf{E}|^2(\phi)$, and that the intensity is independent of ϕ when $\theta_0 = 0$.

Figures 1 through 4 show the internal and external (incident plus scattered) fields at the grain surface, for a couple illustrative cases.

3. Efficiency Factors

In this section, we describe the computation of efficiency factors for scattering, extinction, force, and torque. The calculation of the direct radiative torque is needed for comparison with the photoelectric and photodesorption torques. The other efficiency factors will be used to validate our PMM code (§3.2).

3.1. Definitions and Formulae

The scattering efficiency factor $Q_{\rm sca}$ is defined by

$$P_{\rm sca} = F_{\rm inc} Q_{\rm sca} \pi a_{\rm eff}^2 \tag{54}$$

where $P_{\rm sca}$ is the scattered power and $F_{\rm inc}$ is the incident flux. The scattered power is found by integrating the flux in the scattered fields over a sphere at infinity, yielding (Morrison & Cross 1974; Al-Rizzo & Tranquilla 1995)

$$Q_{\rm sca} = \frac{4}{(k_0 a_{\rm eff})^2} \sum_{n,m}^{m\geq 0} \epsilon_m \frac{n(n+1)}{2n+1}\frac{(n+m)!}{(n-m)!}\left[|a_{nm}(1)|^2 + |a_{nm}(2)|^2\right] \quad ; \tag{55}$$

$\epsilon_m = 1$ (2) for $m = 0$ ($m > 0$).

The extinction efficiency factor $Q_{\rm ext}$ is defined in the same way as $Q_{\rm sca}$ (eq. 54), except that

$P_{\rm sca}$ is replaced by $P_{\rm abs} + P_{\rm sca}$, where $P_{\rm abs}$ is the absorbed power. From the optical theorem,

$$Q_{\rm ext} = \frac{4}{(k_0 a_{\rm eff})^2} {\rm Im} \left\{ \sum_{n,m}^{m \geq 0} \epsilon_m (-i)^n (-1)^m \left[a_{nm}(1) \sin\theta_0 P'(\cos\theta_0) - \frac{m a_{nm}(2) P(\cos\theta_0)}{\sin\theta_0} \right] \right\} \quad \text{(TM)} \tag{56}$$

$$Q_{\rm ext} = \frac{4}{(k_0 a_{\rm eff})^2} {\rm Im} \left\{ \sum_{n,m}^{m \geq 0} i\epsilon_m (-i)^n (-1)^m \left[a_{nm}(2) \sin\theta_0 P'(\cos\theta_0) - \frac{m a_{nm}(1) P(\cos\theta_0)}{\sin\theta_0} \right] \right\} \quad \text{(TE)} \tag{57}$$

(Al-Rizzo & Tranquilla 1995). The absorption efficiency factor $Q_{\rm abs} = Q_{\rm ext} - Q_{\rm sca}$.

The force, or pressure, efficiency factor $\mathbf{Q}_{\rm pr}$ is defined by

$$\mathbf{F}_{\rm rad} = \pi a_{\rm eff}^2 u_{\rm rad} \mathbf{Q}_{\rm pr} \tag{58}$$

where $\mathbf{F}_{\rm rad}$ is the force on the grain and $u_{\rm rad}$ is the incident radiation field energy density. The torque efficiency factor $\mathbf{Q}_\Gamma$ is defined by

$$\mathbf{\Gamma}_{\rm rad} = \pi a_{\rm eff}^2 u_{\rm rad} \frac{\lambda}{2\pi} \mathbf{Q}_\Gamma \tag{59}$$

where $\mathbf{\Gamma}_{\rm rad}$ is the torque and λ is the wavelength of the radiation.

Farsund & Felderhof (1996) derived expressions for the force and torque when the incident and scattered waves are expanded in vector spherical wave functions. Since their conventions differ somewhat from ours, we briefly review some relevant results. First, the incident plane wave is given by

$$\mathbf{E}_{\rm inc} = \sum_{n,m} \left[p_{nm} \mathbf{N}_{nm} + q_{nm} \mathbf{M}_{nm} \right] \tag{60}$$

For the TM mode,

$$p_{nm} = -d_{nm} \sin\theta_0 P'(\cos\theta_0) \quad ; \quad q_{nm} = d_{nm} m P(\cos\theta_0) / \sin\theta_0 \tag{61}$$

and for the TE mode,

$$p_{nm} = -im d_{nm} P(\cos\theta_0) / \sin\theta_0 \quad ; \quad q_{nm} = i d_{nm} \sin\theta_0 P'(\cos\theta_0) \quad ; \tag{62}$$

$$d_{nm} = i^{n+1} (-1)^m \frac{2n+1}{n(n+1)} \frac{(n-m)!}{(n+m)!} \quad . \tag{63}$$

For the TM mode, the coefficients that appear in eqs. (7.25) through (7.30) in Farsund and Felderhof are given by

$$c^i_{hnm} = \frac{-im d_{nm} P(\cos\theta_0)}{k_0 \sin\theta_0} \tag{64}$$

$$c^i_{enm} = \frac{-d_{nm} \sin\theta_0 P'(\cos\theta_0)}{k_0} \tag{65}$$

$$c^s_{hnm} = \frac{i\alpha_m a_{n,|m|}(2)}{k_0}\left[\frac{4\pi}{2n+1}\frac{(n+|m|)!}{(n-|m|)!}\right]^{1/2} \tag{66}$$

$$c^s_{enm} = \frac{\beta_m a_{n,|m|}(1)}{k_0}\left[\frac{4\pi}{2n+1}\frac{(n+|m|)!}{(n-|m|)!}\right]^{1/2} \tag{67}$$

with $\alpha_m = (-1)^{|m|}$ (-1) for $m < 0$ ($m \geq 0$) and $\beta_m = (-1)^{|m|}$ (1) for $m < 0$ ($m \geq 0$).

For the TE mode,

$$c^i_{hnm}(\mathrm{TE}) = -c^i_{enm}(\mathrm{TM}) \quad ; \quad c^i_{enm}(\mathrm{TE}) = c^i_{hnm}(\mathrm{TM}) \tag{68}$$

and the expressions for c^s_{hnm} and c^s_{enm} are the same as for the TM mode, except for an additional negative sign when $m < 0$.

To compute the efficiency factors $\mathbf{Q}_{\rm pr}$ and $\mathbf{Q}_\Gamma$, the expressions in equations (61) through (68) are substituted into the Farsund & Felderhof (1996) expressions for the force and torque (their eqs. 7.25 through 7.30).

3.2. Results

In Figures 5 through 10, we display computational results for the efficiency factors, for a prolate grain, with $\zeta = 3/2$, and an oblate grain, with $\zeta = 2/3$. We take $a_{\rm eff} = 0.2\mu$m and several values of θ_0, the angle between the incident radiation field and the grain's symmetry axis. We adopt dielectric functions for "astronomical silicate" from Draine (2003). Here, and throughout the paper, we assume unpolarized incident radiation; thus, we average over the TE and TM modes. Although the force has a component perpendicular to $\mathbf{k}_0$, we only display $Q_{\rm pr} \equiv \mathbf{Q}_{\rm pr} \cdot \hat{k}_0$. The torque always lies along $\hat{y}$, and vanishes when $\cos\theta_0 = 0$ or 1. (Recall the definition of the coordinate system, in the paragraph following eq. 10.)

For various values of ζ, λ, and θ_0, we have also computed the efficiency factors using the discrete dipole approximation code DDSCAT (version 6.1, Draine & Flatau 2004). In all cases, the results were identical, to within uncertainties associated with incomplete convergence. We encountered no obstacles in convergence with the PMM code, though in some cases we had to take $n_{\rm max} = 80$ to converge to within 1%. For some wavelengths, we were unable to converge to within 10% with DDSCAT, due to limitations on the size of the dipole arrays when using the GNU Fortran compiler. This successful comparison, using two completely different methods, validates both our PMM code and DDSCAT.

For a given incident radiation field, the spectrally averaged force and torque efficiency factors are given by

$$\bar{\mathbf{Q}}_{\rm pr} = \frac{1}{u_{\rm rad}}\int \mathbf{Q}_{\rm pr}\, u_\nu\, d\nu \tag{69}$$

$$\bar{\mathbf{Q}}_\Gamma = \frac{1}{\bar{\lambda}\, u_{\rm rad}}\int \mathbf{Q}_\Gamma\, \lambda\, u_\nu\, d\nu \quad , \tag{70}$$

where ν is the frequency, u_ν is the specific energy density, and $\bar{\lambda} = \int \lambda\, u_\nu d\nu / u_{\rm rad}$. In Figure 11, we display $\bar{Q}_{\Gamma,y}$ for the average interstellar radiation field (ISRF) spectrum in the solar neighborhood, as estimated by Mezger, Mathis, & Panagia (1982) and Mathis, Mezger, & Panagia (1983). (See eq. 31 in Weingartner & Draine 2001b for a convenient representation of the ISRF.) Interestingly, the torque due to radiation with $\lambda > 1\mu$m substantially cancels the torque due to radiation with $\lambda < 1\mu$m. For the ISRF, $u_{\rm rad} = 8.63 \times 10^{-13}\,{\rm erg\,cm^{-3}}$ and $\bar{\lambda} = 1.20\mu$m.

Both the wavelength-dependent and spectrally-averaged efficiency factors are comparable in magnitude to those for the irregular grain studied by Draine & Weingartner (1996); compare figs. 9 and 10 with their fig. 7 and fig. 11 with their fig. 12.

For a spherical silicate grain with $a_{\rm eff} = 0.2\mu$m exposed to the ISRF, $\bar{Q}_{pr} = 0.82$. For spheroids with $\zeta = 2/3$ (3/2), $\bar{Q}_{\rm pr}$ ranges from 0.78 to 0.89 (0.73 to 0.85), with larger values corresponding to larger cross-sectional areas. The transverse component of $\mathbf{Q}_{\rm pr}$ takes values as high as ≈ 0.1.

4. Photoelectric Forces and Torques

4.1. A Simple Model

For simplicity, we will assume that (1) the grains are electrically neutral, (2) the photoelectrons emerge along the surface normal $\hat{n}$, and (3) the photoelectron energy $E_e = h\nu - W$, where $h\nu$ is the incident photon energy and W is the work function of the grain material. Weingartner & Draine (2001b) estimated that silicate grains with $a_{\rm eff} = 0.2\mu$m in the cold neutral medium have a slight positive charge. The rate at which photoelectrons are ejected and the average energy per photoelectron are both lower for positively charged grains than for neutral grains. Thus, each of these simplifications results in an overestimate of the force and torque.[1] This is appropriate for our exploratory study, since we are only attempting to ascertain whether or not the photoelectric torque may be important enough, compared with the direct radiative torque, to warrant further consideration in studies of grain alignment. We will adopt $W = 8\,{\rm eV}$ and the photoelectric yield Y (i.e., the probability that a photoelectron is ejected following the absorption of a photon)

$$Y = 0.5\frac{h\nu - W}{5h\nu - 4W} \quad ; \tag{71}$$

these are the estimates of Weingartner & Draine (2001b) for bulk silicate. On theoretical grounds, it is expected that the yield and ionization potential for a grain with $a_{\rm eff} = 0.2\mu$m deviate little from their bulk values (e.g., Watson 1972, 1973). However, scant experimental evidence on photoelectric emission from sub-micron grains is available. The recent experiment of Abbas et al. (2006) found that the yields of such grains substantially exceed the bulk yield. The work function and yield have

[1] In the rare environments where the grains are highly charged, these may be overestimated by over an order of magnitude (Weingartner & Draine 2001a).

not been well characterized experimentally, even for bulk silicate. Thus, our results for the force and torque will only be rough estimates, and we are justified in making the above simplifications.

Following Kerker & Wang (1982), we will take the photoemission rate as a function of position on the surface proportional to the internal field intensity evaluated at the grain surface, $|\mathbf{E}_{\rm int}^{\rm surf}|^2$. With this assumption, as well as those in the preceding paragraph, the photoelectric force $\mathbf{F}_{\rm pe}$ and torque $\mathbf{\Gamma}_{\rm pe}$ are given by

$$\mathbf{F}_{\rm pe} = \pi a_{\rm eff}^2 u_{\rm rad} \mathbf{Q}_{\rm pr,\,pe} \tag{72}$$

$$\mathbf{\Gamma}_{\rm pe} = \pi a_{\rm eff}^2 u_{\rm rad} \frac{\lambda}{2\pi} \mathbf{Q}_{\Gamma,\,\rm pe} \tag{73}$$

with

$$\mathbf{Q}_{\rm pr,\,pe} = \frac{cQ_{\rm abs}}{h\nu} Y p_e \mathbf{A}_{\rm pr} \tag{74}$$

$$\mathbf{Q}_{\Gamma,\,\rm pe} = \frac{cQ_{\rm abs}}{h\nu} Y p_e \frac{2\pi a_{\rm eff}}{\lambda} \mathbf{A}_{\Gamma} \tag{75}$$

$$\mathbf{A}_{\rm pr} = -\frac{\int |\mathbf{E}_{\rm int}^{\rm surf}|^2 \, \hat{n} \, dS}{\int |\mathbf{E}_{\rm int}^{\rm surf}|^2 \, dS} \tag{76}$$

$$\mathbf{A}_{\Gamma} = -\frac{\int |\mathbf{E}_{\rm int}^{\rm surf}|^2 \, \mathbf{r} \times \hat{n} \, dS}{a_{\rm eff} \int |\mathbf{E}_{\rm int}^{\rm surf}|^2 \, dS} \quad ; \tag{77}$$

p_e is the photoelectron momentum.

The unit surface normal

$$\hat{n} = [1 + (\zeta^4 - 1)\sin^2\theta]^{-1/2} \left[\zeta^2 \sin\theta \, (\hat{x}\cos\phi + \hat{y}\sin\phi) + \hat{z}\cos\theta\right] \tag{78}$$

and the area element

$$dS = r^2 \, \sin\theta \left[1 + \left(\frac{r}{a}\right)^4 \left(1 - \zeta^2\right)^2 \sin^2\theta \, \cos^2\theta\right]^{1/2} d\theta \, d\phi \quad . \tag{79}$$

4.2. Results

The photoelectric torque, like the direct radiative torque, always lies along $\hat{y}$ and vanishes when $\cos\theta_0 = 0$ and 1. Figure 12 displays the y-component of the torque asymmetry factor $\mathbf{A}_\Gamma$ for two values of the incident radiation wavelength λ, both lying within the relevant 8 eV to 13.6 eV spectral range.

In estimating the maximum value of the photoelectric torque, we will take $|A_{\Gamma,y}| \approx 0.05$, independent of λ (fig. 12). We will also take $Q_{\rm abs} \approx 1$, a reasonable approximation when the photon energy exceeds 8 eV (figs. 5 and 6). Defining the spectrally-averaged efficiency factor as in equation (70), we find that $\bar{Q}_{\Gamma,\,\rm pe,\,y} \approx 3.8$. The energy density in the ISRF between 8 eV and 13.6 eV is $u(> 8\,\mathrm{eV}) = 3.86 \times 10^{-14}\,\mathrm{erg\,s^{-1}}$ and $\bar{\lambda} = 0.124\mu$m for this spectral range. From Figure

11, $|\bar{Q}_{\Gamma,y}|$ reaches values as high as ≈ 0.05 for the ISRF. Comparing the radiative and photoelectric torques at the θ_0 for which they peak, we find that $\Gamma_{\rm pe} \approx 0.35\,\Gamma_{\rm rad}$.

If the photoelectric yield varies across the grain surface, then the torque is no longer confined to lie along $\hat{y}$, raising the possibility that even symmetric shapes like spheroids could experience radiation-driven alignment (Purcell 1979). In this case, equation (77) for $\mathbf{A}_\Gamma$ is modified, with the yield Y appearing in both integrals. The z-component of $\mathbf{A}_\Gamma$ remains zero, since the z-component of $\mathbf{r} \times \hat{n}$ always vanishes. Specifically, we situated a single large spot on the grain surface where the yield is enhanced by 10%. When the spot is on the illuminated side of the grain, $A_{\Gamma,\,y}$ changes by as much as $\approx 20\%$ and $|A_{\Gamma,\,x}|$ (and $|A_{\Gamma,\,y}|$ for $\cos\theta_0 = 0,\ 1$) reach values as high as ≈ 0.005. Thus, for real interstellar grains, the aligning torque associated with non-symmetric shape likely dominates any aligning torque associated with non-uniform photoelectric yield.

The forward-direction force asymmetry parameter $A_{\rm pr} \equiv \mathbf{A}_{\rm pr} \cdot \hat{k}_0 \approx 0.4$ to 0.6, while that for the transverse direction ranges from zero to ≈ 0.15. With $A_{\rm pr} \approx 0.5$ and $Q_{\rm abs} \approx 1$, the ISRF spectrally-averaged efficiency factor $\bar{Q}_{\rm pr,\,pe} \approx 3.7$, yielding $F_{\rm pe} \approx 0.2\,F_{\rm rad}$.

5. Photodesorption

Although uncertainties abound in modelling the photoelectric force and torque, photodesorption presents even greater challenges, as described in §4 of Weingartner & Draine (2001a). A major question is whether or not adsorbed H atoms can diffuse across the surface, by either thermal barrier hopping or quantum mechanical tunneling. This depends on the poorly known surface-adatom binding energy.

For uniform surface properties, the magnitude of the photodesorption torque increases with increasing surface coverage of adatoms. Since we seek to estimate the maximum plausible photodesorption torque, we assume complete coverage across the entire surface. This results, for example, if the adatoms do not desorb and the rate at which gas-phase atoms collide with the grain greatly exceeds the removal rates (due to H_2 formation as well as photodesorption).

Photodesorbed H atoms are produced at a rate $\lesssim R^0_{\rm pd} S/l^2$, where $R^0_{\rm pd}$ is the photodesorption rate per adatom, S is the grain surface area, and l^2 is the surface area per binding site. We adopt the crude estimate from Weingartner & Draine (2001a) of $R^0_{\rm pd} \approx 2\times10^{-10}\,{\rm s}^{-1}$ for grains exposed to the ISRF, and we take $l^2 \approx 10\,{\rm \AA}^2$. We also assume that the kinetic energy of photodesorbed atoms is comparable to that of photoelectrons, i.e., $\sim$ eV. Finally, we assume that the photodesorption rate as a function of position on the surface is proportional to the electric intensity just above the surface.

The ratio of the photodesorption torque $\mathbf{F}_{\rm pd}$ to the photoelectric torque can then be simply

estimated as

$$\frac{F_{\rm pd}}{F_{\rm pe}} \sim \frac{S}{\pi a_{\rm aeff}^2} \frac{R_{\rm pd}^0 h\nu}{cu_{\rm rad} Q_{\rm abs} Y l^2} \left(\frac{m_{\rm H}}{m_e}\right)^{1/2} \frac{|\mathbf{A}_\Gamma({\rm pd})|}{|\mathbf{A}_\Gamma({\rm pe})|} \quad , \tag{80}$$

where $S \approx 4\pi a_{\rm eff}^2$ for $\zeta = 3/2$ and $2/3$, $m_{\rm H}$ is the proton mass, $\mathbf{A}_\Gamma({\rm pe})$ is the asymmetry parameter given in equation (77), and $\mathbf{A}_\Gamma({\rm pd})$ is identical, except that the internal electric field $\mathbf{E}_{\rm int}^{\rm surf}$ is replaced with the external electric field at the surface, $\mathbf{E}_{\rm ext}^{\rm surf}$. For $\lambda = 0.15\mu$m, $A_{\Gamma,y}({\rm pd})$ differs very little from $A_{\Gamma,y}({\rm pe})$, but for $\lambda = 0.1\mu$m, the external asymmetry factor is as much as three times smaller than the internal asymmetry factor. With $Q_{\rm abs} \approx 1$, $Y \approx 0.07$, and $A_\Gamma({\rm pd}) \approx A_\Gamma({\rm pe})$, $\Gamma_{\rm pd} \approx 0.3\,\Gamma_{\rm pe}$.

The external and internal pressure asymmetry factors are also generally comparable, though the former can be as much as a factor of 2 smaller than the latter. Thus, for the models considered here, $F_{\rm pd}$ and $F_{\rm pe}$ are of comparable magnitude, as Weingartner & Draine (2001a) found for spheres.

6. Conclusion

The goal of this work was to determine whether or not recoil torques must be included in investigations of radiation-driven grain alignment. Our model for the photoelectric torque neglected a few effects that would tend to suppress the torque (§4.1). We found $\Gamma_{\rm pe} \approx 0.35\,\Gamma_{\rm rad}$, suggesting that the photoelectric torque may actually contribute at about the 10% level compared with the direct radiative torque.

However, the photoelectric yield for sub-micron silicate grains is highly uncertain. If the recent experimental results of Abbas et al. (2006) are accurate, then the yield may be substantially larger than we have assumed. This would increase the torque, but not in direct proportion, since higher yield implies higher positive grain charge, which partially suppresses the torque. Yet, we cannot rule out the possibility that the photoelectric torque is of the same order of magnitude as the radiative torque for spheroids. Clearly, additional experiments are needed to better characterize photoelectric emission from sub-micron silicate grains.

We must also acknowledge the possibility that less symmetric grains may experience larger recoil torques than spheroids, even though the direct radiative torques for the spheroids examined here are comparable in magnitude to that for the irregular grain studied by Draine & Weingartner (1996). The computational demands associated with the PMM are much more severe for grains lacking azimuthal symmetry. However, we have found that the near-surface fields for spheroids are extremely smooth (figs. 1 through 4), suggesting that the discrete dipole approximation may yield sufficient resolution for accurate evaluation of the recoil torques. We will pursue this possibility in future work.

The photodesorption torque appears to contribute at most at the 10% level, although it may be more important if our adopted value for the photodesorption rate, $R_{\rm pd}^0$, is too small. In making our simple estimate, we assumed that the surface-adatom binding energy is relatively large ($> 1\,$eV),

but smaller binding energies (as suggested by, e.g., the recent experiment of Perets et al. 2007) may result in a smaller torque. Futher experimental work characterizing the surfaces of amorphous silicates, and the photodesorption rates, is needed before the torque can be reliably estimated. Thus, for now, we recommend that both recoil torques be omitted from detailed studies of radiation-driven alignment.

We are grateful to Bruce Draine and an anonymous referee for helpful comments. JCW is a Cottrell Scholar of Research Corporation. Support for this work, part of the Spitzer Space Telescope Theoretical Research Program, was provided by NASA through a contract issued by the Jet Propulsion Laboratory, California Institute of Technology under a contract with NASA.

REFERENCES

Abbas, M. M. et al. 2006, ApJ, 645, 324

Al-Rizzo, H. M. & Tranquilla, J. M. 1995, J. Computational Phys., 119, 342

Dolginov, A. Z. & Mytrophanov, I. G. 1976, Ap&SS, 43, 291

Draine, B. T. 2003, ApJ, 598, 1026

Draine, B. T. & Flatau, P. J. 2004, http://arxiv.org/abs/astro-ph/0409262

Draine, B. T. & Weingartner, J. C. 1996, ApJ, 470, 551

Draine, B. T. & Weingartner, J. C. 1997, ApJ, 480, 633

Farsund, O. & Felderhof, B. U. 1996, Physica A, 227, 108

Jackson, J. D. 1999, Classical Electrodynamics, 3rd ed. (Wiley)

Kerker, M. & Wang, D.-S. 1982, J. Colloid Interface Sci., 85, 302

Kim, S.-H. & Martin, P.G. 1995, ApJ, 444, 293

Lazarian, A. 2003, J. Quant. Spectrosc. Radiat. Transfer, 79, 881

Lazarian, A. 2007, J. Quant. Spectrosc. Radiat. Transfer, 106, 225

Martin, P. G. 1971, MNRAS, 153, 279

Mathis, J. S., Mezger, P. G., & Panagia, N. 1983, A&A, 128, 212 Mezger, P. G., Mathis, J. S., & Panagia, N. 1982, A&A, 105, 372

Morrison, J. A. & Cross, M. J. 1974, Bell Syst. Tech. J., 53, 955

Perets, H. B. et al. 2007, ApJ, 661, L163

Purcell, E. M. 1979, ApJ, 231, 404

Roberge, W. G. 2004, in ASP Conf. Ser. 309, Astrophysics of Dust, ed. A. N. Witt, G. C. Clayton, & B. T. Draine (San Francisco:ASP), 467

Watson, W. D. 1972, ApJ, 176, 103

Watson, W. D. 1973, J. Opt. Soc. Am., 63, 164

Weingartner, J. C. & Draine, B. T. 2001a, ApJ, 553, 581

Weingartner, J. C. & Draine, B. T. 2001b, ApJS, 134, 263

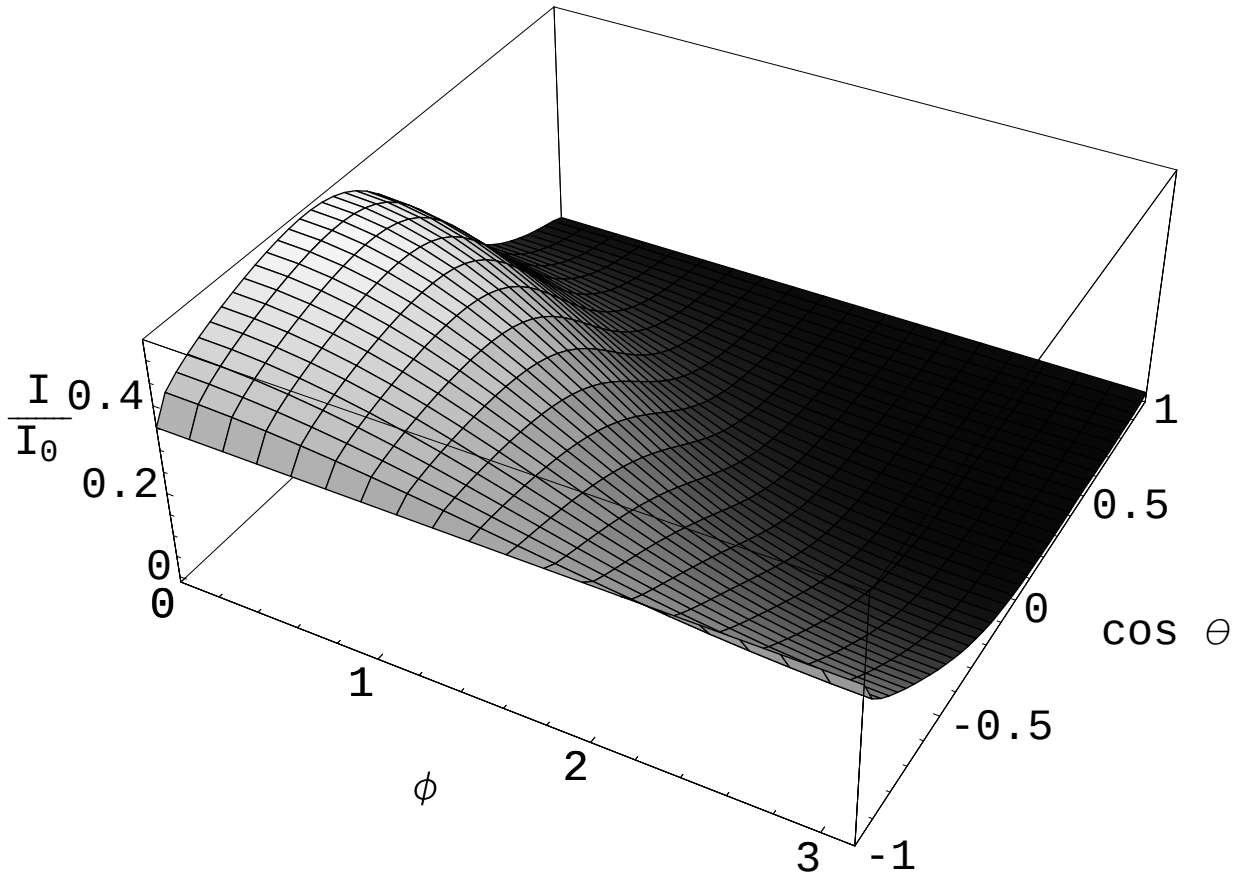

Fig. 1.— The intensity $I = |\mathbf{E}|^2$ of the internal field (averaged over the TE and TM modes and normalized to the incident intensity I_0) at the grain surface, for an oblate ($\zeta = 2/3$) silicate grain with $a_{\rm eff} = 0.2\mu$m, incident wavelength $\lambda = 0.1\mu$m, and angle between the incident radiation and the grain symmetry axis $\theta_0 = \cos^{-1} 0.6$.

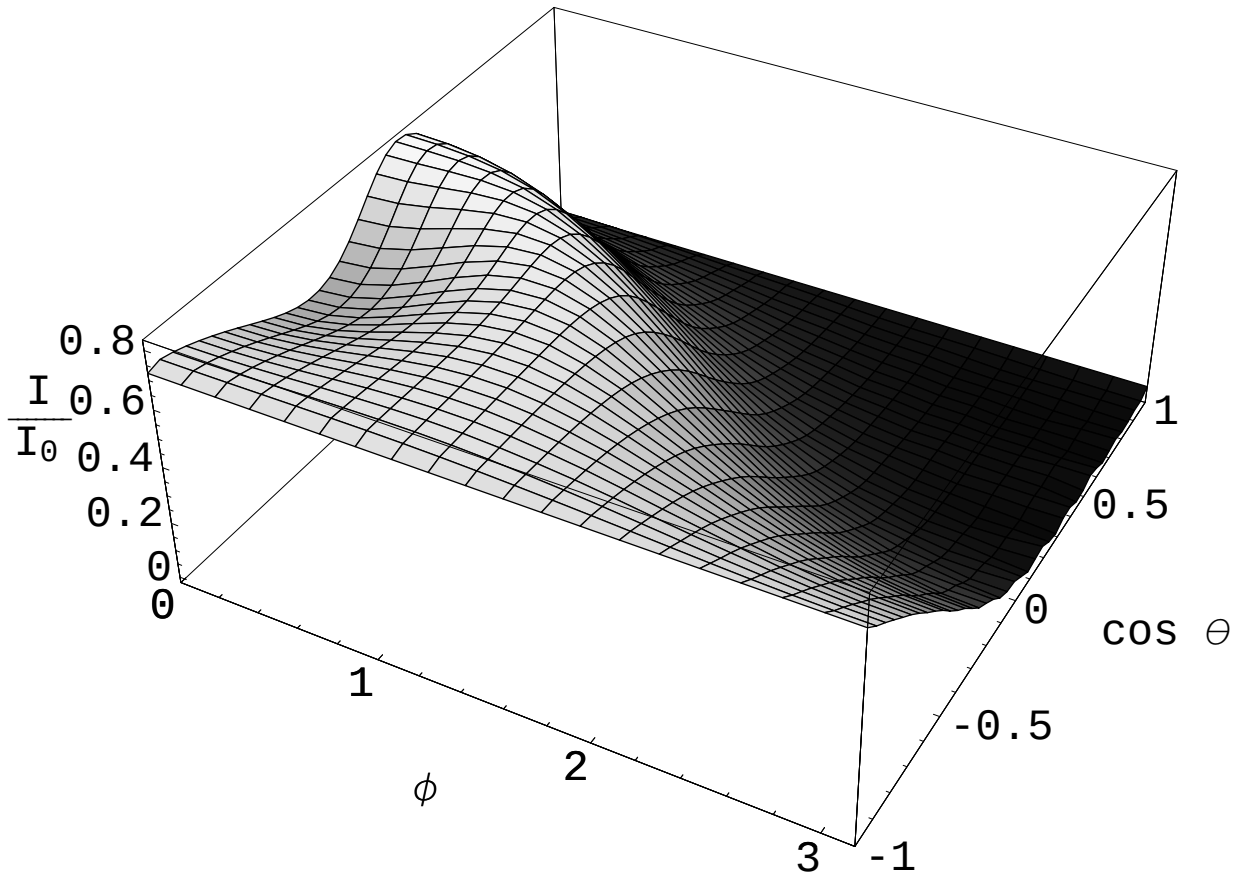

Fig. 2.— Same as fig. 1, except that the external field intensity at the grain surface is plotted.

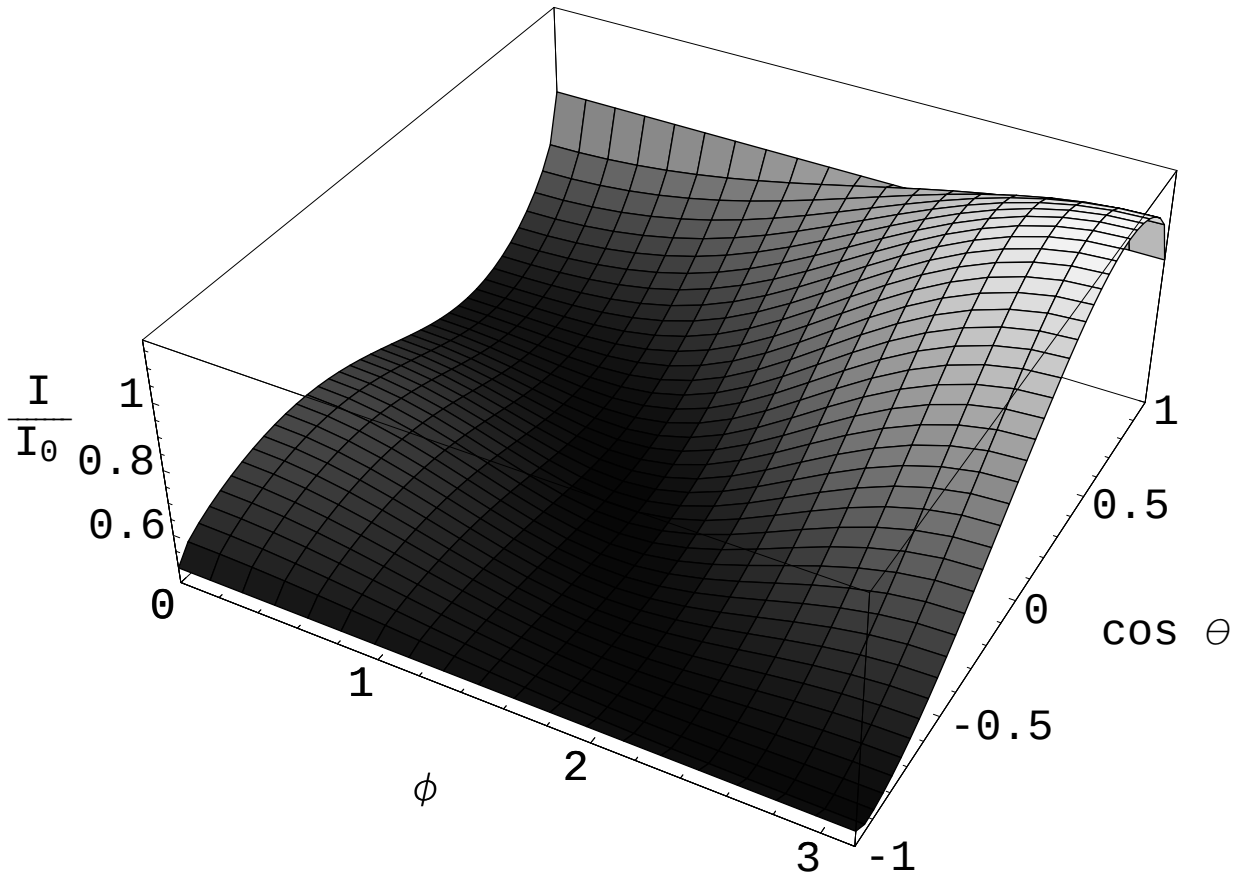

Fig. 3.— Same as fig. 1, except that $\lambda = 1\mu$m.

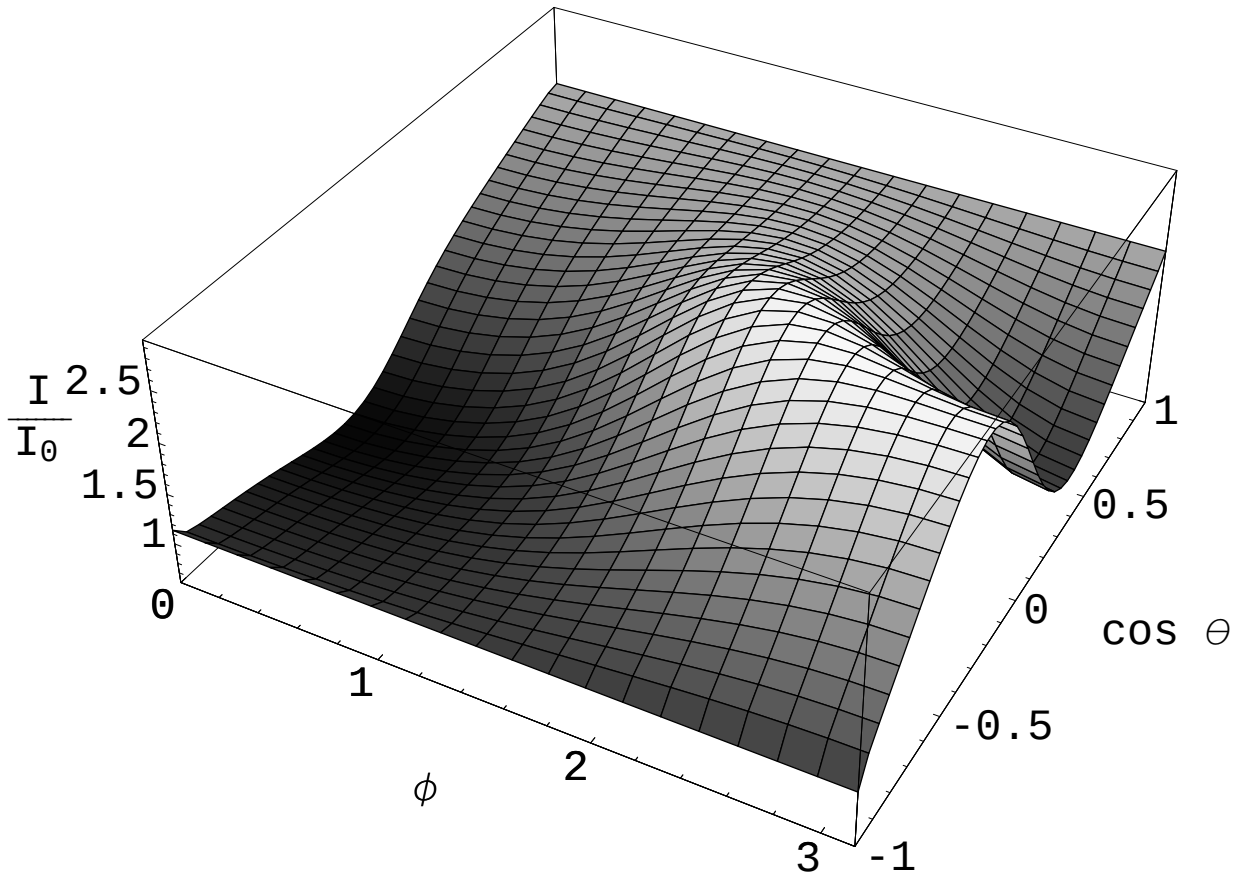

Fig. 4.— Same as fig. 2, except that $\lambda = 1\mu$m.

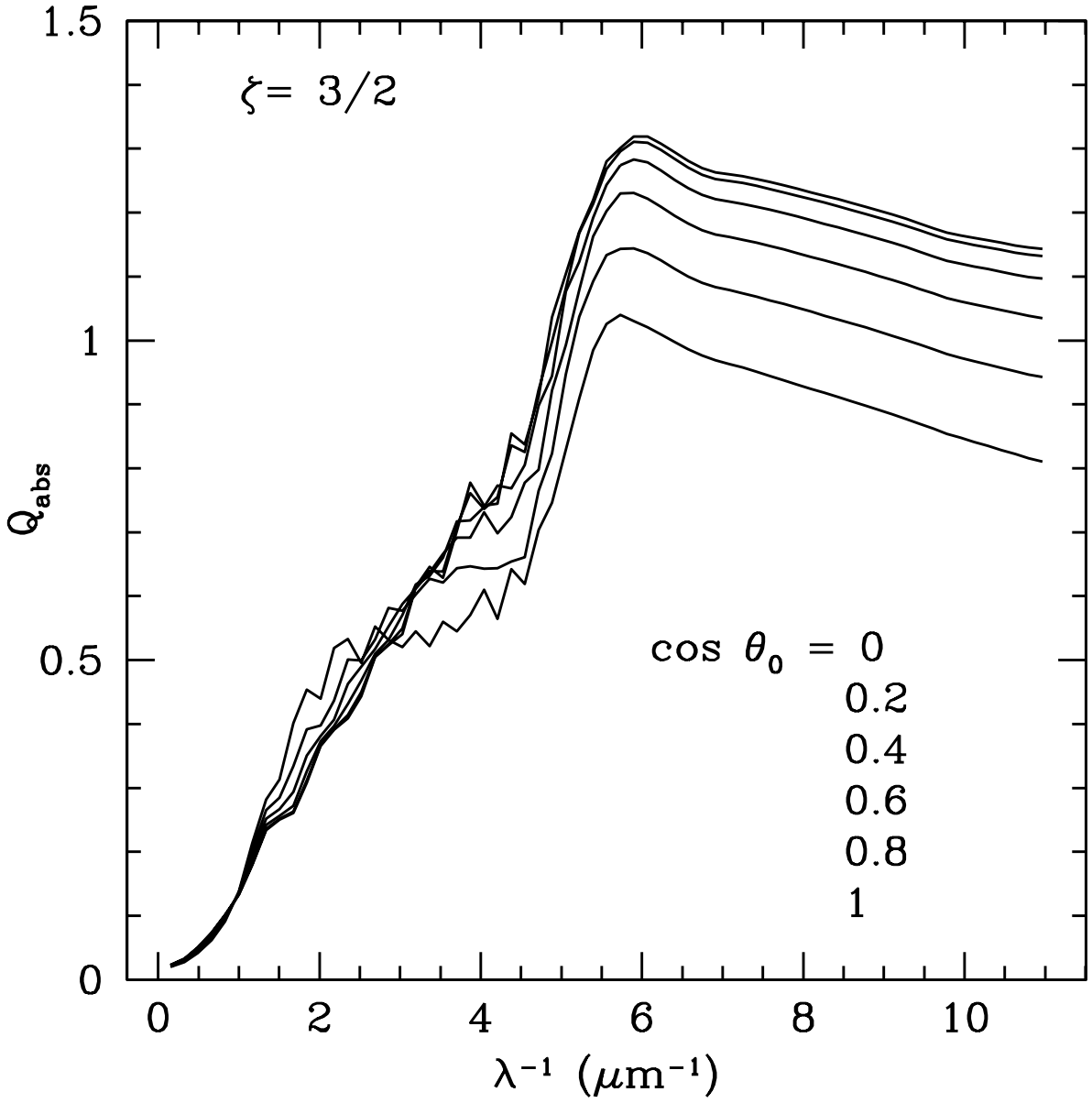

Fig. 5.— $Q_{\rm abs}$ for prolate ($\zeta = 3/2$) grains with $a_{\rm eff} = 0.2\mu$m and various values of θ_0.

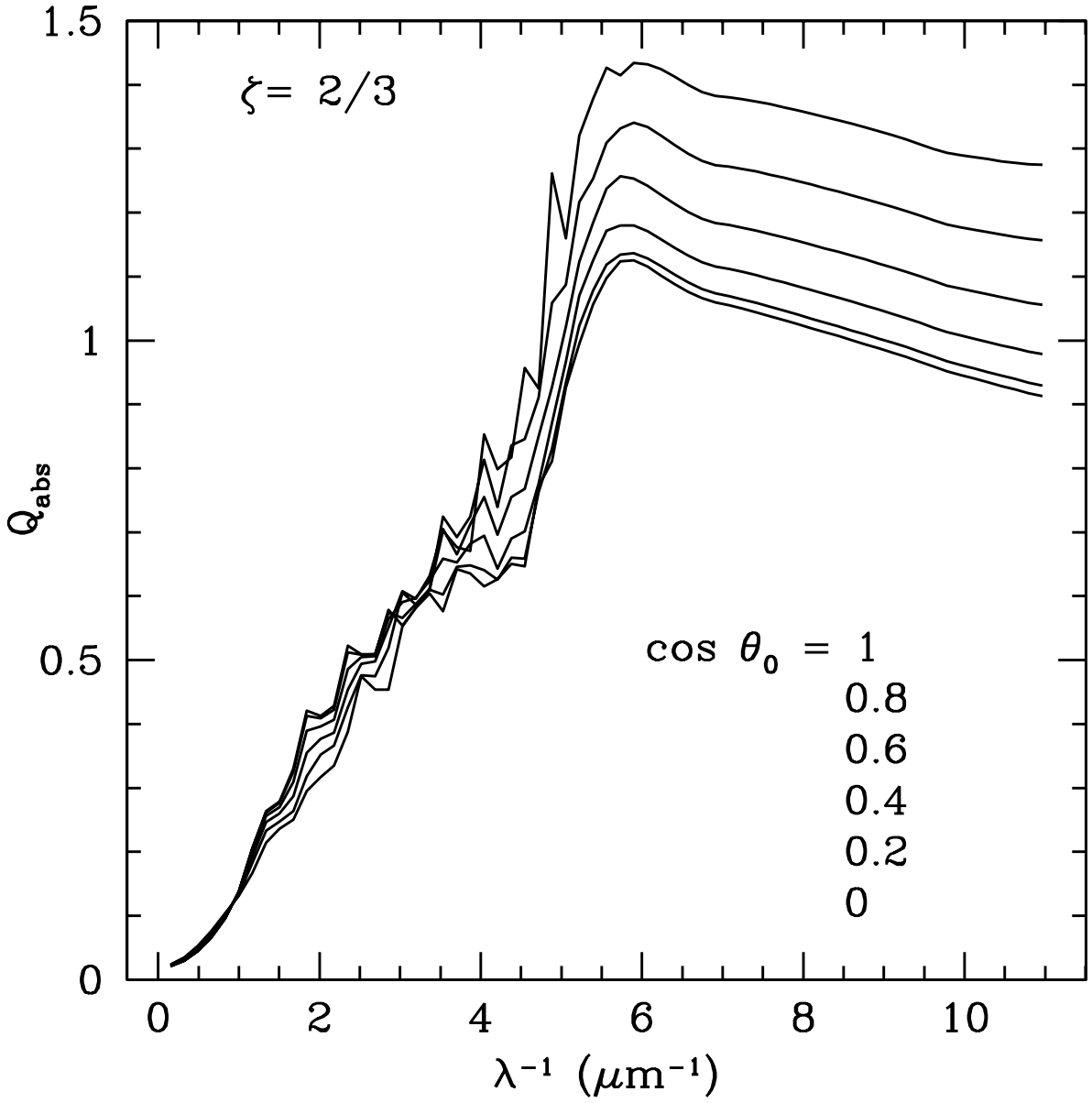

Fig. 6.— $Q_{\rm abs}$ for oblate ($\zeta = 2/3$) grains with $a_{\rm eff} = 0.2\mu$m.

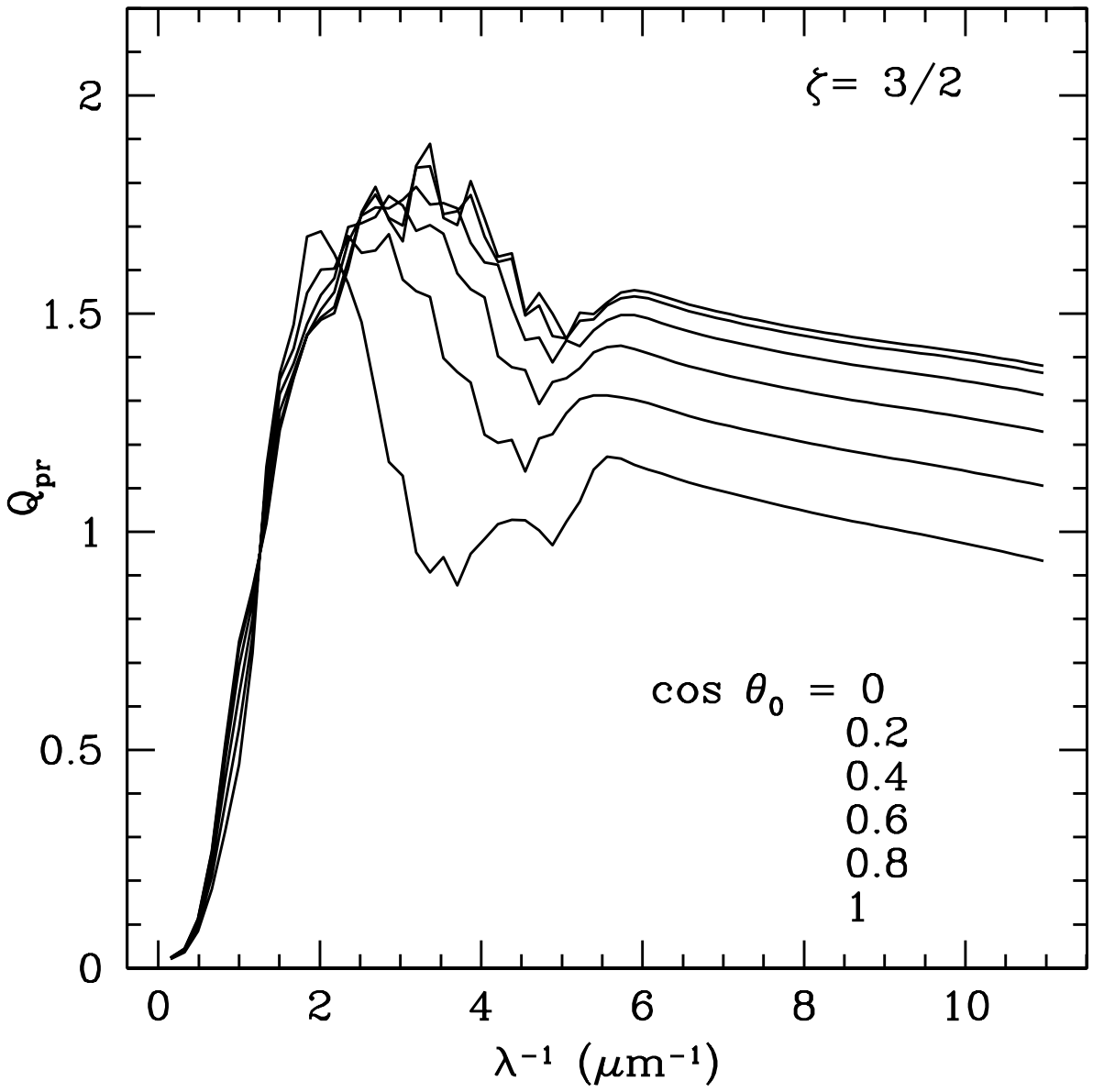

Fig. 7.— $Q_{\rm pr}$ for prolate ($\zeta = 3/2$) grains with $a_{\rm eff} = 0.2\mu$m.

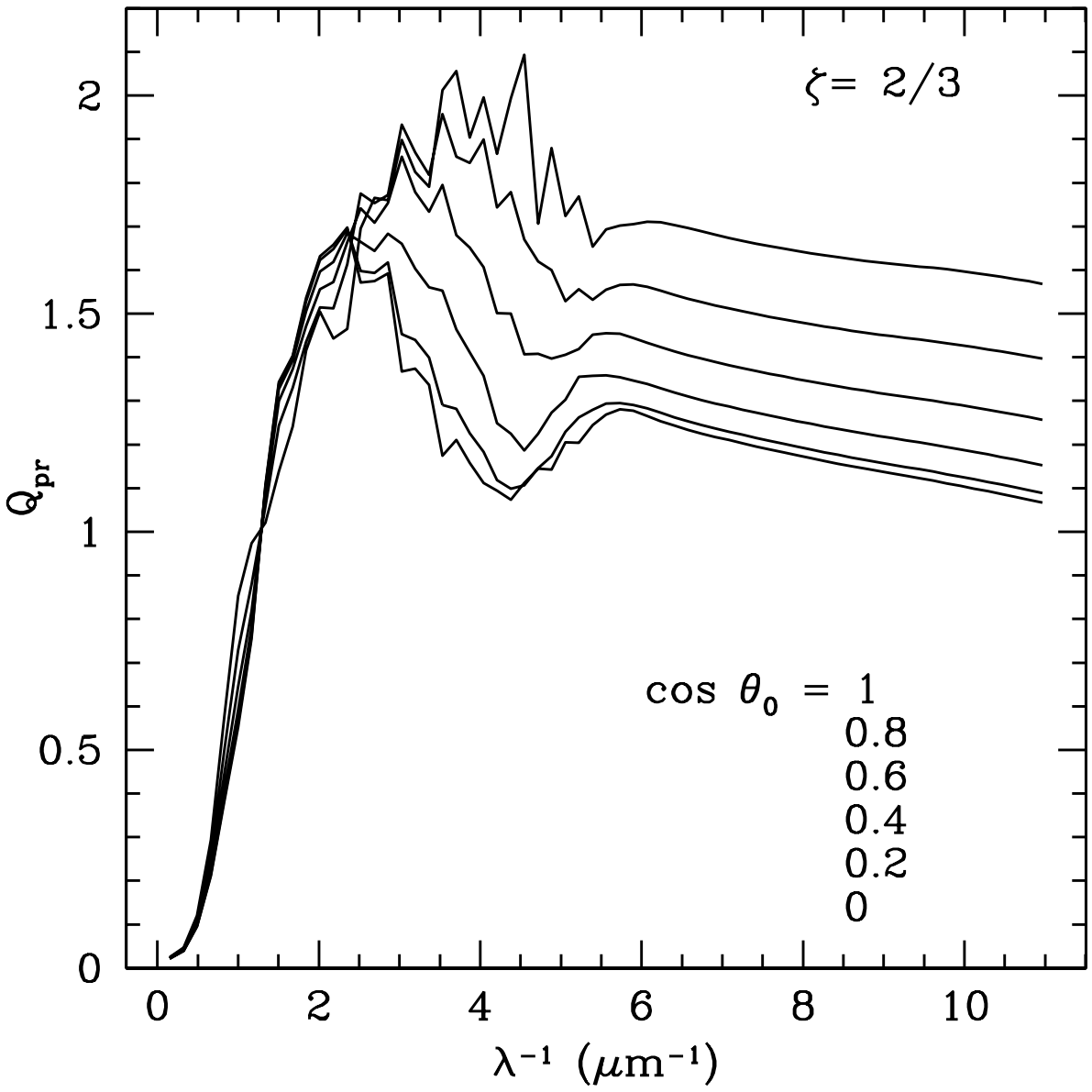

Fig. 8.— $Q_{\rm pr}$ for oblate ($\zeta = 2/3$) grains with $a_{\rm eff} = 0.2\mu$m.

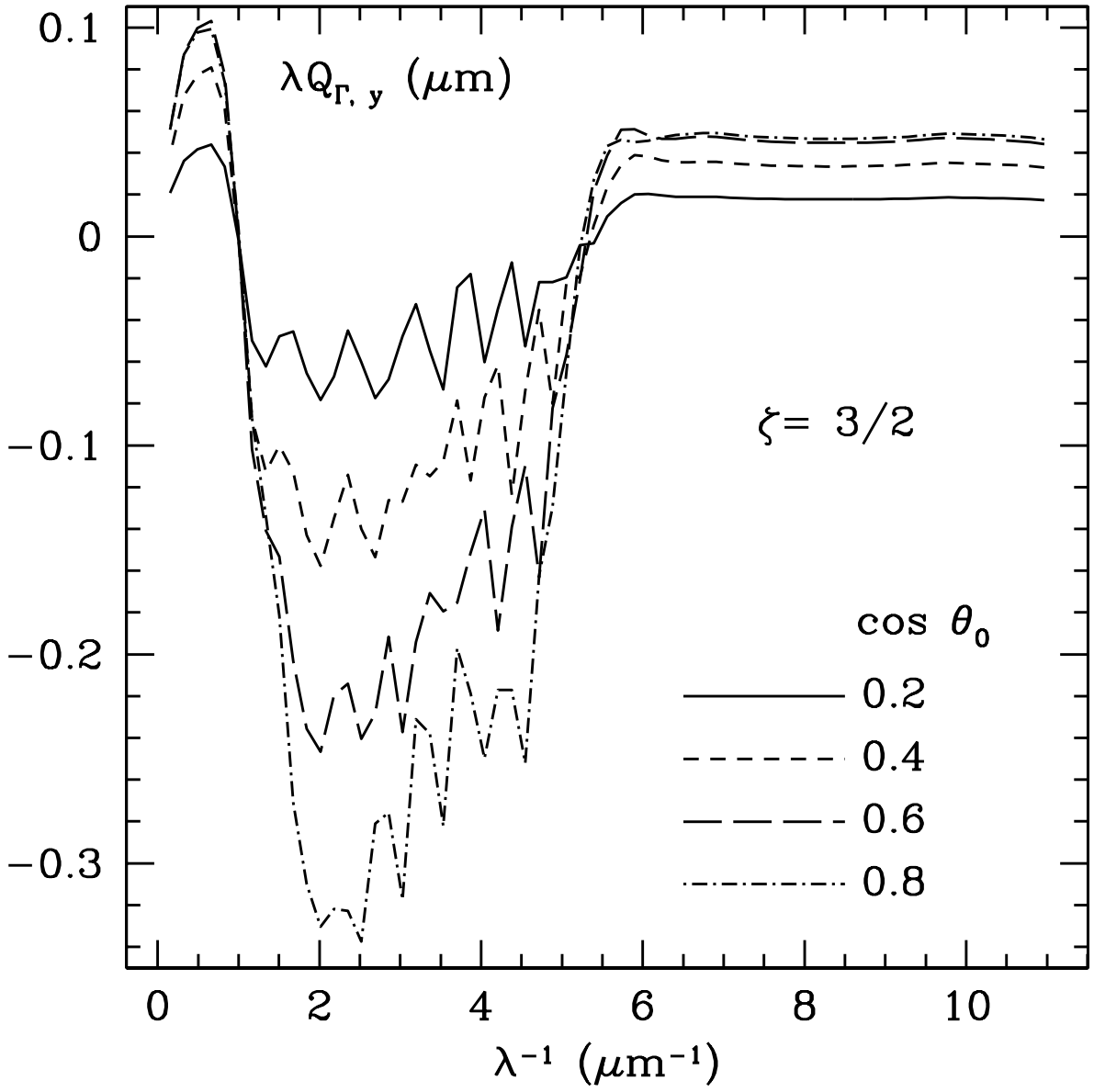

Fig. 9.— $\lambda Q_{\Gamma,y}$ for prolate ($\zeta = 3/2$) grains with $a_{\rm eff} = 0.2\mu$m.

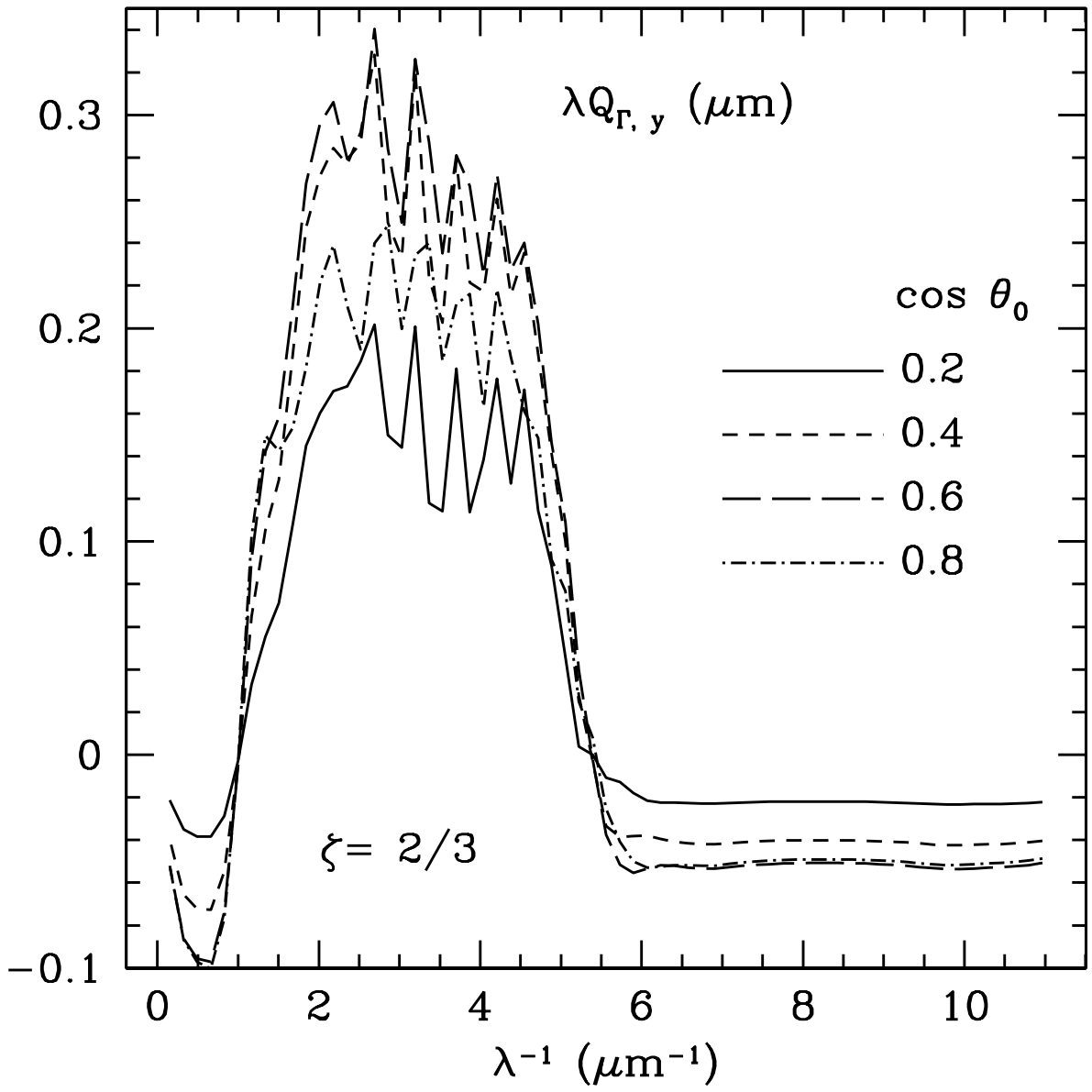

Fig. 10.— $\lambda Q_{\Gamma,y}$ for oblate ($\zeta = 2/3$) grains with $a_{\rm eff} = 0.2\mu$m.

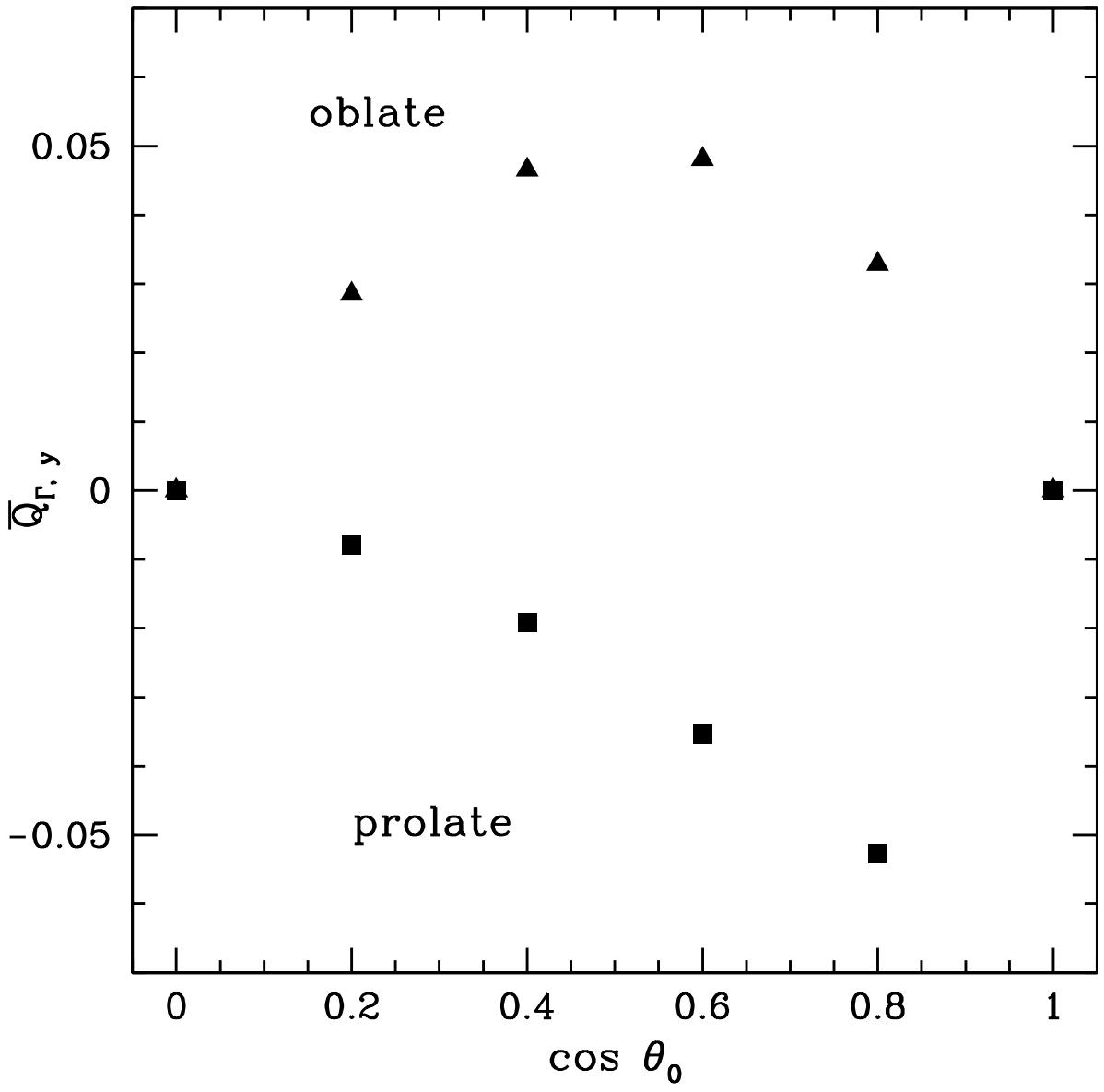

Fig. 11.— The torque efficiency factor averaged over the MMP radiation field, $\bar{Q}_{\Gamma,y}$, for prolate ($\zeta = 3/2$) and oblate ($\zeta = 2/3$) grains with $a_{\rm eff} = 0.2\mu$m.

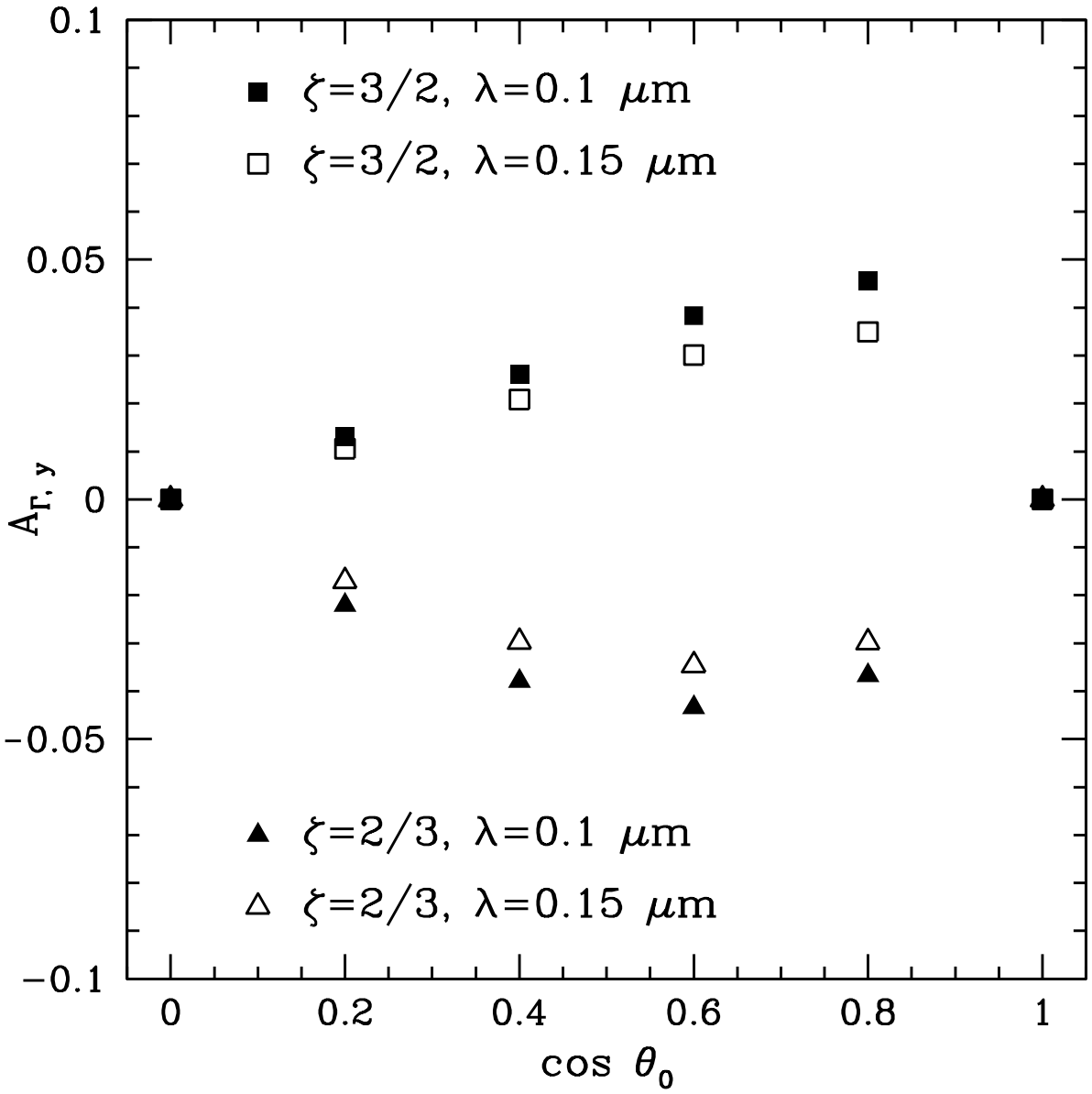

Fig. 12.— The y-component of the torque asymmetry factor $\mathbf{A}_\Gamma$.